Microwave-assisted hydrothermal synthesis of Mn$_3$O$_4$/reduced graphene oxide composites for high power supercapacitors

Chien-Liang Liu, Kuo-Hsing Chang, Chi-Chang Hu*, Wei-Chung Wen

Laboratory of Electrochemistry and Advanced Materials, Department of Chemical Engineering, National Tsing Hua University, No. 101 Kuang-Fu Road, Hsin-Chu 30013, Taiwan

HIGHLIGHTS

► Mn$_3$O$_4$/RGO composites with controllable composition are fabricated by a MAHS method.
► Mn$_3$O$_4$/RGO composites show 81% C$_{S,T}$ retention by varying the scan rate from 0.025 to 1 V s^{-1}.
► A Mn$_3$O$_4$/RGO/N-doped GS asymmetric EC shows 11 Wh kg^{-1} and 24 kW kg^{-1} at 24 A g^{-1}.
► The aqueous asymmetric EC shows capacitor behavior with a cell voltage of 2 V.

ARTICLE INFO

ABSTRACT

Crystalline hausmannite nanocrystals/reduced graphene oxide composites (denoted as Mn$_3$O$_4$/RGO) are synthesized by means of the microwave-assisted hydrothermal synthesis (MAHS) route for the application of symmetric and asymmetric supercapacitors. Effects of the Mn$_3$O$_4$ content on the microstructure and electrochemical performances of nanocomposites are systematically investigated. The morphology and crystalline structure of composites are examined by scanning electron microscopic (SEM) and X-ray diffraction (XRD) analyses. Thermogravimetric analysis (TGA) is used to determine the mass content of RGO in the Mn$_3$O$_4$/RGO composites. The results indicate that the composite with about 82.4 weight percents (wt%) Mn$_3$O$_4$ (denoted as GMn80) shows the largest total specific capacitance ($\sim$193 F g^{-1}), which is employed for the tests of supercapacitors of both symmetric and asymmetric types. An aqueous asymmetric supercapacitor, consisting of a GMn80 cathode and an N-doped RGO anode (reduced from a GO-NH$_4$OH solution through the MAHS method), with a cell voltage of 2 V is demonstrated in this work, which shows the device energy and power densities of 11.11 Wh kg^{-1} and 23.5 kW kg^{-1}, respectively.

1. Introduction

Manganese oxides of various oxidation states/structures were attractive to considerable research interest due to their promising application potentials in several fields, such as catalytic oxygen reduction [1], ion exchange [2], molecular adsorption [3], magnetic applications [4], and electrochemical energy storage devices [5–8]. For instance, Mn$_3$O$_4$ has been reported to be a promising catalyst for oxygen reduction in the metal-air batteries [1]. In addition, MnO$_2$ is widely reported to be a promising electrode material in both alkaline batteries and electrochemical supercapacitors, which undergoes redox transitions between different oxidation states to store and deliver electric energy [5,6,8]. In the recent decade, amorphous MnO$_x$ (denoted as a-MnO$_x$) prepared by both co-precipitation and electrochemical deposition was found to exhibit ideal capacitive behavior in neutral, aqueous electrolytes [5,8]. This important finding attracts greater interest in both synthesis and characterization of various manganese oxides for this high-power application. However, contractions in both electrochemical and textural properties are commonly found. For example, a-MnO$_2$ prepared by chemical co-precipitation was firstly announced as an electrode material for the supercapacitor application while its capacitive performances cannot be obtained if electronic conductivity of the resultant electrode matrix is not suitably promoted (e.g., by adding 20% carbon) [9]. On the other hand, non-stoichiometric a-MnO$_x$ prepared by anodic and potentiodynamic deposition was clearly demonstrated to be responsible for these excellent capacitive properties [5,10]. The charge storage process of a-MnO$_2$ was reported to follow a very similar mechanism of

* Corresponding author. Tel./fax: +886 3 5736027.
  E-mail address: cchu@che.nthu.edu.tw (C.-C. Hu).
  URL: http://mx.nthu.edu.tw/~cchu/

hydrous RuO_2 (i.e., the double injection/expel of cations/protons and electrons) [11]. Due to the exchange of Na^+ and electrons [8,12], crystalline Na_xMnO_2 was also shown to be an electroactive species for the charge storage/delivery. On the other hand, Mn oxides in the other structures (e.g., Mn_3O_4, MnOOH, etc.) have also been reported to exhibit capacitive-like responses, while electrochemical activation seems to be a key step for promoting the capacitive performances of such oxides [13]. Furthermore, adding Mn_3O_4 into Mn oxide-based composites was reported to be an important factor to maintain excellent charge–discharge stability [14].

Based on the above findings, Mn_3O_4 is a promising electrode material for the supercapacitor application, which is one of the most stable manganese oxides, and shows a variety of important applications [15–17]. However, Mn_3O_4 generally shows low electrical conductivity. To find a material to complement this drawback is hence highly demanded. Consequently, a great deal of research has been launched into combining Mn_3O_4 with conducting substrates such as activated carbon fibers to gain better electrochemical performances [18]. Due to the better electronic conductivity and higher specific surface area of reduced graphene oxide (RGO) in comparing with activated carbon fibers and carbon nanotubes, introducing RGO sheets into Mn_3O_4 is believed to effectively overcome the above issue meanwhile the utilization of active materials can be significantly enhanced by uniform dispersion of Mn_3O_4 nanocrystals onto RGO sheets. Accordingly, RGO-based Mn_3O_4 composites show high competition on enhancing the pseudocapacitive performances due to the significant merits owned by RGO and a combination of RGO and Mn_3O_4 will be promising electrode materials of supercapacitors. Even so, synthesis of Mn_3O_4/RGO composites still went through complicated processes. A facile and simple method to synthesize Mn_3O_4/RGO composites is a challenge. Hence, supercapacitors consisting of Mn_3O_4/RGO composites as the electrode material are worthwhile to be investigated [18–20].

Reduced graphene oxide, very similar to graphene sheets, a two-dimensional sheet of covalently bonded carbon atoms, exhibits high electronic conductivity, low mass density, very high theoretical specific surface area (2630 m^2 g^{-1}) [21] and can be employed for a multitude of applications [22]. The very high in-plane conductivity and surface area make it an attractive material for use in dye sensitized solar cells [23], supercapacitors [24], and other applications. Recently, extensive research has focused on the development of metal oxides/RGO composites for the electrode materials of supercapacitors and batteries, because the ultrathin flexible RGO layers can serve to be a support for anchoring well-dispersed metal oxide nanoparticles and work as a highly conductive matrix [25–27]. The resultant nanocomposites are expected to possess synergic effects from both components, such as enhancement in electronic conductivity and specific capacitance.

For practical applications in the future, advanced supercapacitors of high cell voltages must be developed in order to promote their energy density without sacrificing the power delivery ability and cycle life [28]. Although activated carbon-based electrical double layer capacitors (EDLCs) with organic electrolytes exhibit very long cycle life, the power and energy densities need to be improved [29]. To circumvent the above issues, supercapacitors of the asymmetric (hybrid) type have been explored by combining a battery-like Faradaic electrode (as the energy source) and a capacitive electrode (as the power source) to offer combined merits of supercapacitors (i.e., high rate and long cycle-life) and batteries (high energy density) [30–32]. Asymmetric supercapacitors make use of the different potential windows of the two electrodes coated with different active materials to enlarge the operation cell voltage which leads to a notable improvement in the

energy density of electrochemical supercapacitors for approaching the energy density of rechargeable batteries [31,33,34] while a sacrifice in the power delivery ability and/or cycle life has been found for such a combination [28].

Based on all the above viewpoints, developing a simple and facile process for synthesizing Mn_3O_4/RGO composites with desired microstructures (e.g., crystal size control and uniform dispersion/anchoring of Mn_3O_4 as well as smooth electron and cation pathways) is still a challenge. In this work, microwave-assisted hydrothermal synthesis (MAHS) is proposed to fabricate N-doped RGO and Mn_3O_4/RGO composites with the above desired microstructures for Mn_3O_4-based asymmetric supercapacitors. The unique merits of MAHS include (1) time-saving, (2) simple (similar to hydrothermal synthesis), (3) facile composition control, (4) easy crystal size and phase control, (5) uniform dispersion/anchoring of oxides, and (6) high production efficiencies (>95%). In addition, not only graphene oxide can be reduced to RGO but also Mn_3O_4 nanocrystals will be converted from Mn hydroxide precipitated on the surface of RGO in this MAHS process. Furthermore, due to the excellent microwave absorption ability of GO and RGO, well crystalline Mn_3O_4 anchored on RGO in aqueous media and nitrogen doping on RGO in a simple NH_4OH solution can be achieved by this method. Hence, the nanocomposite with ca. 82.4 wt% Mn_3O_4 (denoted as GMn80) shows the highest total specific capacitance (~193 F g^{-1}) and fantastic capacitance retention (~81%) when the scan rate is increased from 25 to 1000 mV s^{-1}. Finally, the performances of a symmetric GMn80 supercapacitor and an asymmetric supercapacitor consisting of a GMn80 cathode and an N-doped RGO anode (with a cell voltage of 2 V) are systematically compared to demonstrate the obvious enhancements in both energy and power densities by using the asymmetric design.

2. Experimental details

Graphene oxide (GO) was prepared via the Hummer's method [35], i.e., the natural graphite powder was oxidized with $KMnO_4$ in concentrated H_2SO_4. First, 0.25 g graphite powders were added into 10 mL 98% H_2SO_4 and, then 1 g $KMnO_4$ and 0.25 g $NaNO_3$ were added gradually while stirring. The above mixture was ultrasonicated for 1 h and then, 20 mL deionized water was added slowly into the mixture. The reaction was terminated by adding a 10-mL 5% H_2O_2 solution. The solid product was separated via centrifugation, washed repeatedly with deionized water. Afterward, the powders collected were well dispersed in deionized water.

Different amounts of $MnCl_2$ were dissolved in 10 mL deionized water. This solution was mixed with a 10-mL, as-prepared GO solution with stirring and pH of the resultant solution was adjusted to be 11 by adding 0.1 M NaOH. The above precursor solutions were transferred to a microwave reactor (CEM, USA) to form Mn_3O_4/RGO composites under a constant power of microwave (100 W) at 200 °C for 10 min. There are four samples with different Mn_3O_4 contents, which were denoted as GMn55, GMn65, GMn80 and GMn90, respectively. Nitrogen-doped reduced graphene oxide (N-doped RGO) was prepared from an aqueous 20-mL solution containing 0.8 M NH_4OH, 110 g L^{-1} ethylene glycol (EG), and 1000 mg L^{-1} GO. The above precursor solutions were transferred to a microwave reactor (CEM, USA) to form N-doped RGO under a constant power of microwave (100 W) at 160 °C for 10 min. The resultant composite and N-doped RGO powders were filtered, washed with deionized water repeatedly, and finally kept in a vacuum oven at 85 °C overnight.

The pretreatment procedure of the 10 × 10 × 3 mm graphite supports (Nippon Carbon EG-NPL, N.C.K.) completely followed our

previous work [36,37]. The exposed geometric area of these pre-treated graphite supports is equal to 1 cm^2 and the other surface areas were coated with PTFE (polytetrafluorene ethylene) films. The material for the working electrode was a mixture consisting of Mn_3O_4/RGO and PVdF (polyvinylidene difluoride) in a weight ratio of 19:1. The mixture was homogeneously suspended in N-methyl-2-pyrrolidone, which was coated on a graphite substrate with an exposed surface area of 1 cm^2. The mass loading of active materials on all electrodes was carefully controlled to be ca. 0.5 mg cm^{-2}.

The scanning electron microscopic (SEM) images of Mn_3O_4/RGO composites were obtained by a field-emission scanning electron microscope (Hitachi S-4700I, Japan). X-ray diffraction patterns of Mn_3O_4/RGO composites were measured from an X-ray diffractometer (CuK, Ultima IV, Rigaku) at an angular speed of (2θ) 1° min^{-1}. The crystal size of Mn_3O_4 is estimated from the full width at half-maximum (FWHM) from the strongest peak centered at 35.04° on all XRD patterns by means of the Scherrer equation. The RGO content of composites was determined by thermogravimetric analysis (TGA, TA Instruments SDT Q600), which was performed in an air flow at 10 °C min^{-1} from room temperature to 500 °C.

The electrochemical performances of Mn_3O_4/RGO composites were investigated by CHI 633C (CH Instruments, USA) in a three-compartment cell. An Ag/AgCl electrode (Argenthal, 3 M KCl, 0.207 V vs. standard hydrogen electrode at 25 °C) was used as the reference electrode, and a piece of platinum gauze was employed as the counter electrode. A Luggin capillary was used to minimize errors due to iR drop in the electrolyte. For the two-electrode, full-cell test, CVs and the charge−discharge test were also measured by the same instrument. The working electrode is connected to the cathode meanwhile the counter and reference electrodes were connected to the anode. The electrolyte for evaluating the capaci-tive performances of composites is an aqueous solution containing 0.5 M Na_2SO_4. The electrolyte used for measuring the performances of asymmetric capacitor is the same solution with 5 mM $NaHCO_3$ for enhancing the stability of composites at potentials positive than 0.9 V (vs. Ag/AgCl).

All solutions used in this work were prepared with 18 MΩ cm water produced by a reagent water system (Milli-Q SP, Japan). The electrolytes used for the electrochemical characterization were degassed with purified nitrogen gas before measurements for 25 min and this nitrogen was passed over the solutions during the measurements.

3. Results and discussion

3.1. Textural characteristics

Fig. 1 shows the XRD patterns of all Mn_3O_4/RGO nanocomposites prepared by means of the MAHS method. Note that the diffraction peaks completely match the standard pattern of Mn_3O_4 from a comparison of these patterns with the standard reference (PDF#24-0734). This result indicates that the MAHS method is an easy and time-saving method for fabricating Mn_3O_4/RGO composites. Moreover, the crystal size of Mn_3O_4 in all composites is approximately the same (ca. 18.4 ± 0.4 nm). According to the mechanism proposed previously [13], the amount of Mn hydroxide anchored onto GO should be directly proportional to the MnCl$_2$ content in the precursor solution, which can be effectively trans-formed into Mn_3O_4 nanocrystals under the MAHS environment. Consequently, the larger amount of Mn hydroxide anchored onto GO favors the growth of Mn_3O_4 nucleus, leading to the formation of larger amount of Mn_3O_4 crystals in the Mn_3O_4-enriched compos-ites. Also note that there is no diffraction peak corresponding

to graphite, revealing that Mn_3O_4 crystals in the Mn_3O_4/RGO composites are powerful nano-spacers inhibiting the re-stacking of RGO sheets.

Fig. 2 shows the SEM images of pure Mn_3O_4, Mn_3O_4/RGO composites with different amounts of Mn_3O_4, and pure RGO. From a comparison of all images in Fig. 2, several features need to be mentioned. First, the relatively obscure SEM image of pure Mn_3O_4 (i.e., Fig. 2a) is attributable to its low conductivity in comparing with Mn_3O_4/RGO composites and RGO. Second, the morphologies of GMn55 and RGO are similar (see Fig. 2b and f), attributable to the little amount of Mn_3O_4 nanocrystals uniformly dispersed within GMn55. Third, with increasing the amount of MnCl$_2$ in the precursor solution, more Mn_3O_4 powders anchor on the surface of RGO sheets from an examination of Fig. 2b−d. This result strongly supports the statement that the amount of Mn hydroxide anchored onto GO is proportional to the MnCl$_2$ content in the precursor solution. Accordingly, it is easy to control the amount of Mn_3O_4 nanocrystals in the Mn_3O_4/RGO composite under the MAHS environment. Fourth, for GMn90, the surface of RGO sheets is completely coated with Mn_3O_4 particles (see Fig. 2e). Owing to the too large amount of Mn_3O_4 onto the RGO sheets, the electronic conductivity of GMn90 decreases signifi-cantly, resulting in the unclear SEM image. Based on the above results and discussion, the conductivity of GMn80 is fairly good and should show excellent capacitive performances due to the combination of the pseudocapacitance of Mn_3O_4, the double-layer capacitance of composites, and the good electronic conductivity of RGO.

Fig. 3 shows the typical thermogravimetric analysis (TGA) results for pure Mn_3O_4 and Mn_3O_4/RGO composites with different amounts of Mn_3O_4. The weight loss occurring at temperatures lower than ca. 100 °C is reasonably attributed to the evaporation of physically adsorbed water. The weight loss at temperatures ≤250 °C is generally increased with increasing the RGO content, especially obvious on curves 2 and 3, which is attributable to the total water content (physically adsorbed and chemically bound water). This phenomenon is probably due to the porous nature of RGO sheets, favorable for the adsorption of water molecules, which is commonly found for porous materials [38,39]. From a comparison of all curves in Fig. 3, RGO starts to be decomposed into CO_2 and H_2O at temperatures above 250 °C. Furthermore, Mn_3O_4 will be trans-formed to Mn_2O_3 when the temperature is above 500 °C [40], indicating that Mn_3O_4 is very stable in the temperature region
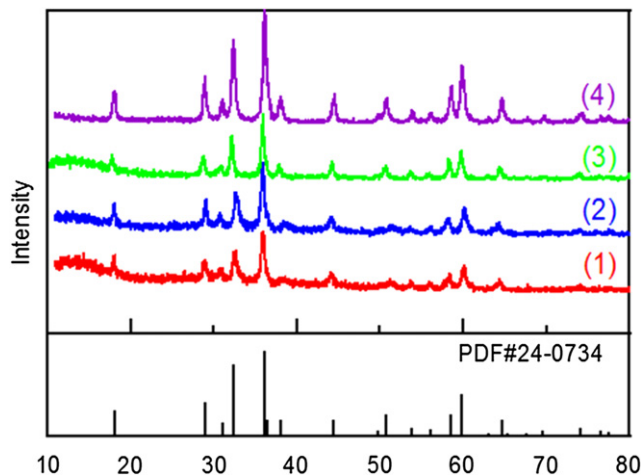

Fig. 1. XRD patterns of (1) GMn55, (2) GMn65, (3) GMn80, (4) GMn90 and the refer-ence pattern of Mn_3O_4 (PDF#24-0734).
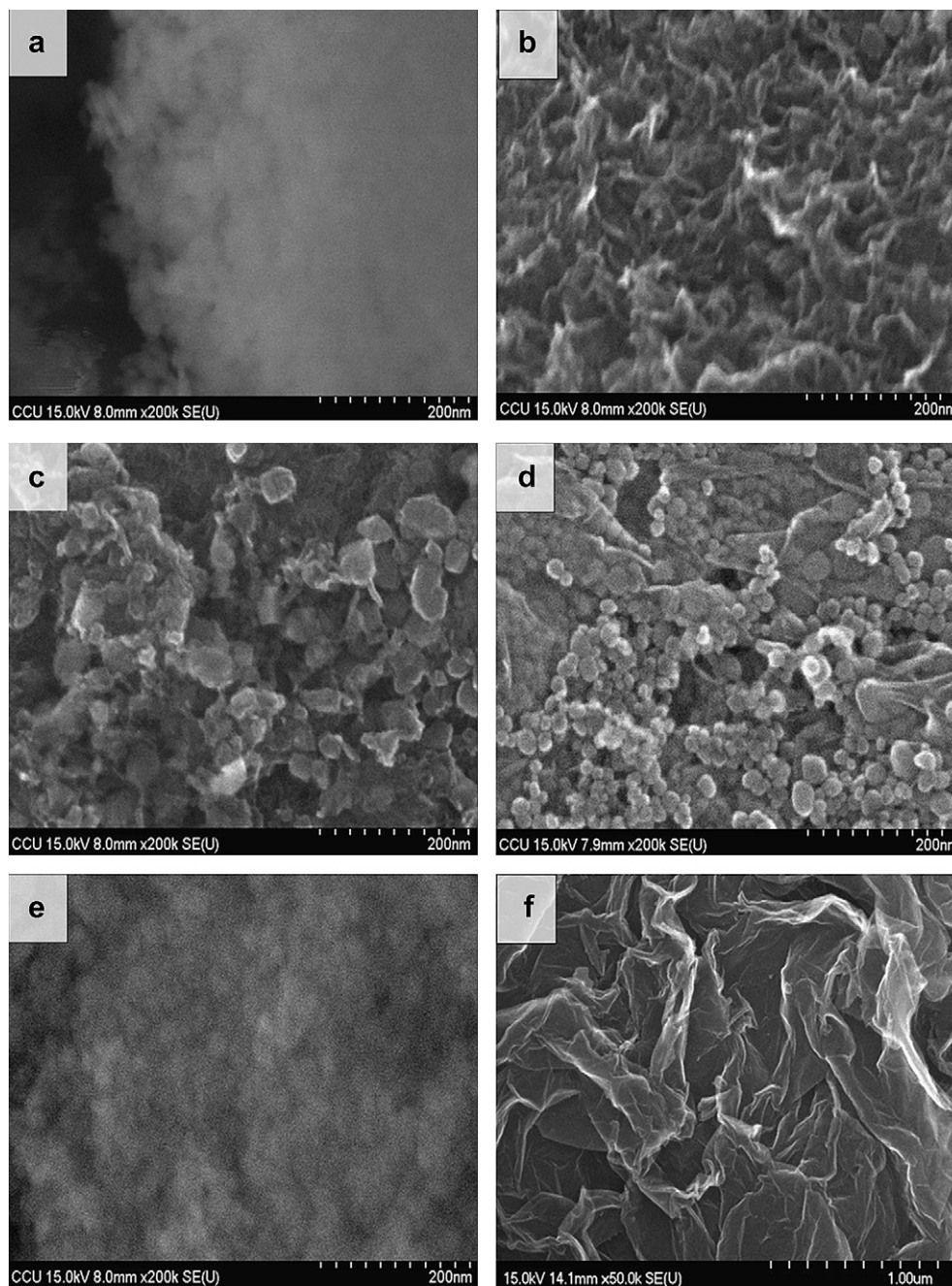
Fig. 2. SEM images of (a) pure Mn_3O_4, (b) GMn55, (c) GMn65, (d) GMn80, (e) GMn90, and (f) RGO.

of TGA. The gradual weight loss on curve 1 for pure Mn_3O_4 at temperatures above 250 °C and the minor weight loss after the large weight reduction on curves 2–5 might be attributed to the surface sintering and/or growth of Mn_3O_4 nanocrystals (e.g., the formation of bridge-type oxygen through $2Mn-O-H \rightarrow Mn-O-Mn + H_2O$) at elevated temperatures although the actual reason responsible for this phenomenon is unclear. Accordingly, the amount of RGO in the composites is reasonably estimated from the weight loss between 250 and 500 °C. Based on this assumption, the amounts of RGO in GMn55, GMn65, GMn80 and GMn90 are equal to 46.1, 35.7, 17.6, and 10.3 wt%, respectively. This result reveals that the amount of Mn_3O_4 nanocrystals in the composites can be controlled by varying the Mn hydroxide content anchored onto GO, which is proportional to the $MnCl_2$ content in the precursor solution.

3.2. Capacitive performances

The capacitive behavior of pure Mn_3O_4, RGO and Mn_3O_4/RGO composites was systematically examined in this work and typical CV curves of pure Mn_3O_4, RGO and GMn80 measured at 25 mV s^{-1} in 0.5 M Na_2SO_4 are shown in Fig. 4a. Note that these three electrode materials generally show capacitive-like behavior in the electrolyte while pure Mn_3O_4 and GMn80 have been potentiodynamically activated for 200 cycles in the same media [13]. The latter phenomenon reveals that Mn_3O_4 with electrochemical activation possesses pseudocapacitive responses in 0.5 M Na_2SO_4, which has been found in our previous study [13]. On the other hand, from a comparison of all curves in Fig. 4a, the order of materials with respect to decreasing the average capacitive current density
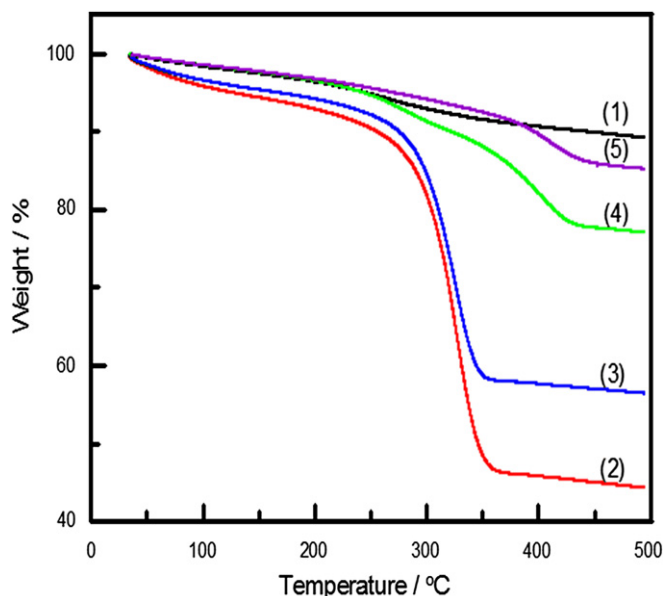
Fig. 3. The TGA curves for (1) Mn_3O_4, (2) GMn55, (3) GMn65, (4) GMn80 and (5) GMn90.

is: GMn80 (5.55 A g^{-1}) > pure Mn_3O_4 (1.76 A g^{-1}) > RGO (1.19 A g^{-1}). Accordingly, a synergistic effect is found by combining Mn_3O_4 and RGO, reasonably resulted from the uniform dispersion of Mn_3O_4 nanocrystals onto the surface of RGO sheets and the good electronic conductivity of RGO. Hence, a high utilization of electroactive species (i.e., Mn_3O_4) can be achieved and the specific capacitance values of pure Mn_3O_4, RGO and GMn80 are equal to 55.4, 32.1 and 193.0 F g^{-1}, respectively. Moreover, the spacer of Mn_3O_4 nanocrystals uniformly dispersed within the conductive RGO network should promote the utilization of the double-layer capacitance of nano-composites. It is worthwhile to mention that GMn80 shows the typical rectangular, capacitive-like behavior, very similar in shape to that of hydrous RuO_2 nanocrystals prepared by means of hydrothermal synthesis [41]. This result can be attributed to the formation of conductive networks of electrons and electrolytes in the Mn_3O_4/RGO composites, resulting in the improvement of reversibility and symmetry of curves. Note that in this work, the total specific capacitance ($C_{S,T}$) of the electrode materials is calculated from the CV curves according to Eq. (1):

$$C_{S,T} = \frac{|Q|}{w \cdot \Delta V} \qquad (1)$$

where $|Q|$, w, and ΔV are indicative of the average voltammetric charges integrated from the positive and negative sweeps, the coating weight of electrode materials, and the potential window of CV, respectively. Due to the considerations of electrochemical reversibility, and stability, the suitable potential window of Mn_3O_4/GS composites for the supercapacitor application in 0.5 M Na_2SO_4 is between 0 and 1 V (vs. Ag/AgCl) [42].

To demonstrate the merits of introducing RGO into Mn_3O_4, Fig. 4b and c show the typical CV curves measured at different scan rates of CV in 0.5 M Na_2SO_4 for GMn80 and GMn90, respectively. In Fig. 4b, all CV curves measured at scan rates varying from 25 to 1000 mV s^{-1} are rectangular-like and highly symmetric, indicating that GMn80 exhibits highly reversible charge and discharge responses in this medium. This highly reversible behavior is seldom
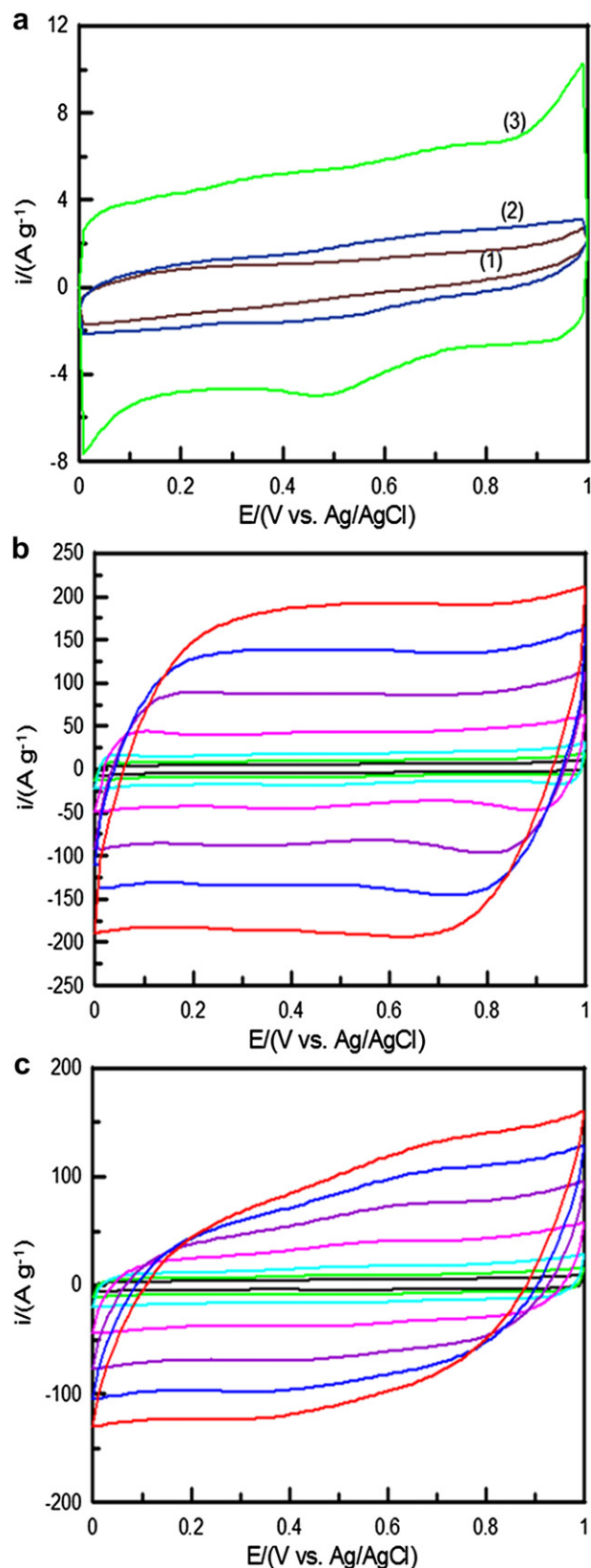

Fig. 4. (a) Cyclic voltammograms of (1) RGO, (2) pure Mn_3O_4, and (3) GMn80 measured at a scan rate of 25 mV s^{-1} in 0.5 M Na_2SO_4 and cyclic voltammograms of (b) GMn80 and (c) GMn90 measured at a scan rate varied from 25 to 1000 mV s^{-1} in 0.5 M Na_2SO_4.

found for Mn oxides because of their poor electronic conductivity [43], which is more obvious when the loading/thickness of Mn oxides becomes higher [44–46]. Accordingly, the current density of CV curves in Fig. 4c is directly proportional to the scan rate of CV at the scan rates of CV ≤200 mV s^{-1}, while the CV curves are significantly distorted, indicating a deviation from the ideal capacitive behavior [47,48], when the scan rates are faster than 200 mV s^{-1}. This result is consistent with the finding that the amount of Mn$_3$O$_4$ in GMn90 is too high to maintain good electronic conductivity (resulting in the unclear SEM image in Fig. 2e) for the very high-rate charge/discharge applications.

Fig. 5 shows the dependence of the total specific capacitance on the amount of Mn$_3$O$_4$ in the composites. Clearly, the total specific capacitance of composites initially increases with increasing the amount of Mn$_3$O$_4$ and reaches a maximum for GMn80 (e.g., the total specific capacitance of pure Mn$_3$O$_4$, GMn55, GMn65, GMn80, and GMn90 measured at 25 mV s^{-1} equal to 55.4, 57.6, 63.3, 193.0, and 175.7 F g^{-1}, respectively). This result indicates that well-dispersed Mn$_3$O$_4$ nanocrystals in RGO not only enhances the utilization of electroactive materials but also promote the spread of RGO nanosheets for increasing the double-layer capacitance of composites because the uniformly dispersed Mn$_3$O$_4$ nanocrystals are able to work as a nanospacer avoiding the re-stacking of RGO nanosheets. In addition, the optimal composition is about 20 wt% RGO in the composite (i.e., GMn80) in order to construct the conductive networks of electrons and electrolyte in the Mn$_3$O$_4$/RGO composites. This statement is supported by the excellent capacitance retention (81%) of GMn80 when the scan rate is changed from 25 to 1000 mV s^{-1}, presented as curve 3 in Fig. 5. From a comparison of all curves in Fig. 5, the loss in the total specific capacitance of GMn55, GMn65, GMn80, and GMn90 is respectively equal to 29.5, 28.9, 37.4, and 91.5 F g^{-1} when the scan rate of CV is varied from 25 to 1000 mV s^{-1}. The low loss in the total specific capacitance for the former three Mn$_3$O$_4$/RGO composites indicates the good electronic conductivity and high porosity of composites, contributed from RGO, for the charge storage and delivery. Since the restacking of RGO is not obviously found for all composites from the XRD patterns shown in Fig. 1, the very obvious decay in the total specific capacitance against the scan rate on curve 4 is reasonably attributed to the relatively poor electronic conductivity of GMn90 due to the overloading of Mn$_3$O$_4$. Hence, the capacitance loss percentage (ca. 52% $C_{S,T}$ loss) for GMn90 is very similar to that for pure Mn$_3$O$_4$ (ca. 54% $C_{S,T}$ loss). On the other hand, the total specific capacitance

of GMn90 measured at 1000 mV s^{-1} is about 84 F g^{-1} which is much higher than that of GMn55, GMn65, and most data of Mn oxide-based materials reported in the literature [49,50]. Based on all the above results and discussion, Mn$_3$O$_4$/RGO composites with suitable amounts of RGO are very promising candidates for the electrode materials of high performance supercapacitors meanwhile GMn80 is the best electrode material among all Mn$_3$O$_4$/RGO composites prepared in this work.

It is worthy to note the more obvious decrease of the total specific capacitance in the low scan rate region in comparison with that in the high scan region. In general, the total specific capacitance of Mn$_3$O$_4$/RGO composites can be qualitatively divided into two parts: outer and inner capacitances. The outer capacitance is contributed by both double-layer capacitance (from oxide and RGO) and superficial redox capacitance. The inner capacitance is due to the redox transition of Mn oxy-hydroxide (activated from Mn$_3$O$_4$) beneath the superficial redox layer since the mean crystal size of Mn$_3$O$_4$ is about 18.5 nm. This concept describing an outer layer of superficial oxy-hydroxyl-Mn species being completely cation-accessible and an inner layer of oxy-Mn species being less cation-accessible is similar to that proposed for RuO$_2$ [51–53]. Due to the well crystalline structure of Mn$_3$O$_4$ prepared by means of MAHS and/or the larger size of hydrated sodium ions (in comparison with proton), the cation diffusion rate to the inner layer of oxy-Mn species should be slow. Consequently, a very obvious decrease of the total specific capacitance in the low scan rate region is found. On the other hand, the outer capacitance is the main contributor to the total specific capacitance in the high scan rate region, which is weakly scan-rate-dependent.

3.3. Performances of symmetric and asymmetric supercapacitors

Based on the results and discussion in previous sections, GMn80 was employed to assemble a symmetric supercapacitor in order to demonstrate its excellent capacitive performances. Due to the possible dissolution of Mn oxide in the higher oxidation state and oxygen evolution at potentials positive than 1.0 V (vs. Ag/AgCl) as well as the irreversible reaction at potentials negative than 0 V (vs. Ag/AgCl) [42], the cell voltage should be equal to/lower than 1.0 V. Fig. 6a shows the typical charge–discharge curves of a symmetric supercapacitor consisting of GMn80 measured at 1.2 A g^{-1} (based on the total mass of GMn80 on both electrodes). Clearly, the symmetry of all charge–discharge curves is excellent, owing to the intrinsic reversibility of GMn80 in the testing electrolyte. Note that the cell voltage of this symmetric supercapacitor can be up to 1.0 V. The galvanostatic charge–discharge curves of the symmetric supercapacitor at different current densities show that the cell voltage is approximately linearly proportional to the charge or discharge time in 0.5 M Na$_2$SO$_4$, indicating a typical capacitor response (see Fig. 6b). Moreover, the ohmic loss (iR drop) is not obvious on all curves, indicating the equivalent series resistance (ESR) is small. The above results demonstrate the promising property of GMn80 for the high-power supercapacitor application. Accordingly, the energy and power densities of such a symmetric cell can be calculated from these charge–discharge curves. The energy and power densities of a full cell can be evaluated on the basis of Eqs. (2) and (3):

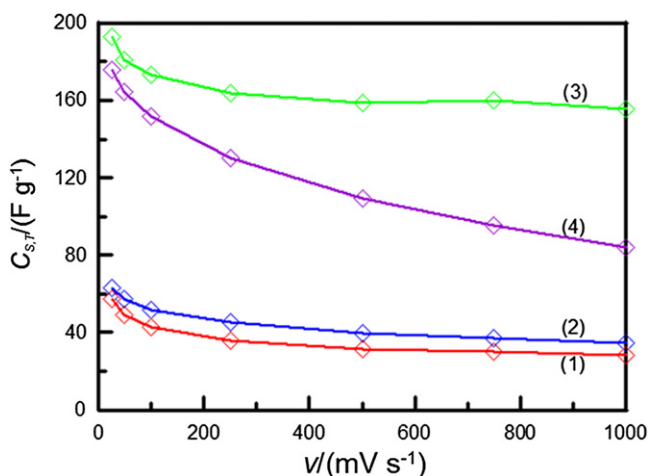$$SE = \frac{CV^2}{2w_T} \qquad (2)$$

$$SP = \frac{SE}{t} \qquad (3)$$

Fig. 5. The dependence of the total specific capacitance of (1) GMn55, (2) GMn65, (3) GMn80, and (4) GMn90 on the scan rate of CV.
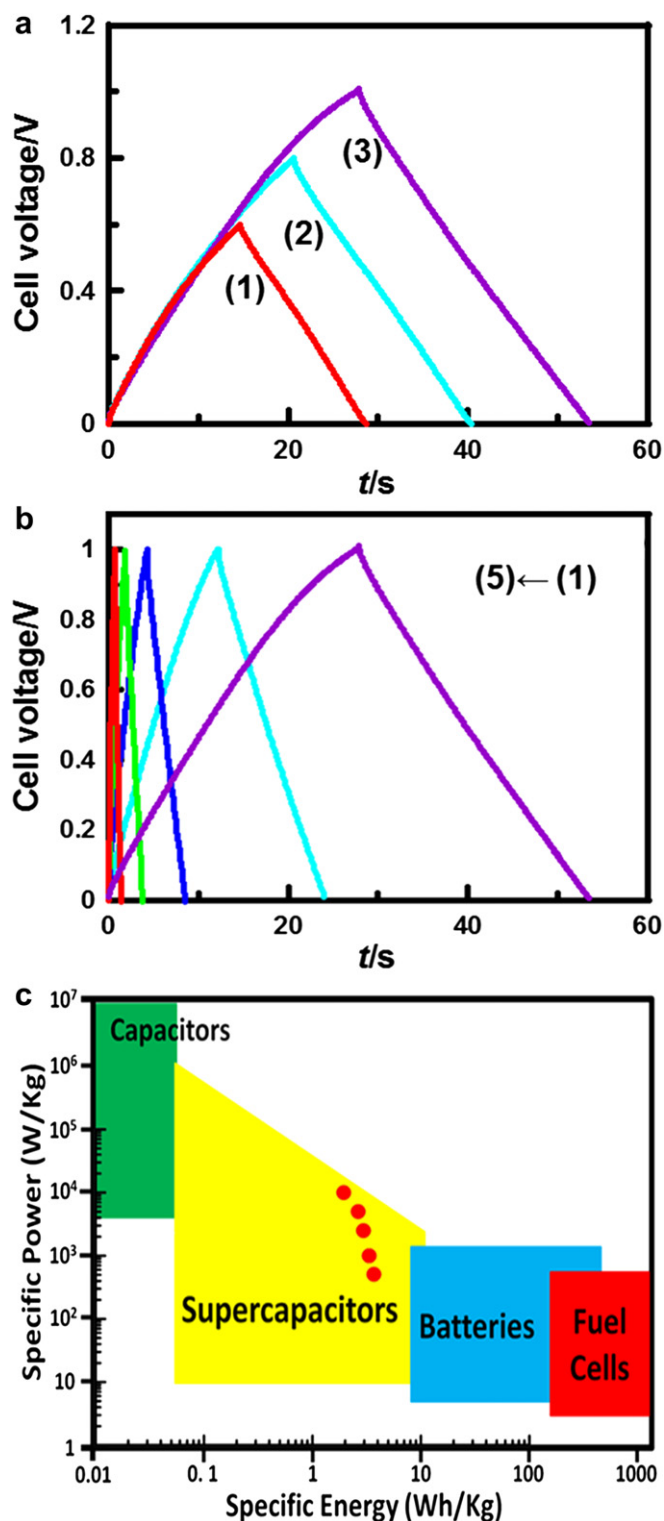
Fig. 6. The constant-current charge–discharge profiles of a symmetric supercapacitor consisting of GMn80 (a) with the cell voltage of (1) 0.6, (2) 0.8, and (3) 1.0 V at 1.2 A g^{-1} and (b) with a cell voltage of 1.0 V at (1) 1.2, (2) 2.4, (3) 6, (4) 12, and (5) 24 A g^{-1}. (c) The Ragone plot of a GMn80 symmetric supercapacitor (red dots). (For interpretation of the references to color in this figure legend, the reader is referred to the web version of this article.)

where SE and SP indicate the energy and power densities, respectively. In addition, V is the cell voltage (1.0 V for this symmetric cell), C is cell capacitance estimated from the charge–discharge curves, and w_T is the total mass of all electroactive materials on the cathode

and anode (i.e., total mass of two GMn80 electrodes). Fig. 6c shows the performances of a GMn80-based symmetric cell with a cell voltage of 1.0 V in the Ragone plot. Clearly, the five points corresponding to this cell are located in the typical performance region of supercapacitors (e.g., 3.7 Wh kg^{-1} and 508 W kg^{-1} at 1.2 A g^{-1}). Moreover, at the extreme operation condition, i.e., at 24 A g^{-1}, the energy and power densities of this cell are equal to ca. 2 Wh kg^{-1} and 9 kW kg^{-1}, respectively, which reaches the upper limit of the typical performance region of supercapacitors (see Fig. 6c). On the other hand, in order to meet the demand of energy and power densities equal to/larger than 10 Wh kg^{-1} and 10 kW kg^{-1} for the supercapacitors of next generation [54,55], enlarging the cell voltage by assembling the supercapacitor of the asymmetric type is an unavoidable way.

To enlarge the cell voltage in order to enhance the energy and power densities of devices, a GMn80 cathode and an N-doped RGO anode are assembled to be an asymmetric supercapacitor. N-doped RGO prepared in this work is employed as the anode material because of the fact that N-doped RGO possesses both high specific capacitance and high power ability in comparing with carbon nanotubes and activated carbons [41,56]. Since adding a little amount of NaHCO$_3$ in the Na$_2$SO$_4$ electrolyte has been found to stabilize Mn oxides in the high positive potential region [42,57], 5 mM NaHCO$_3$ was introduced into the 0.5 M Na$_2$SO$_4$ electrolyte for testing the asymmetric supercapacitors.

Fig. 7a shows the typical CV curves of N-doped RGO and GMn80 in the electrolyte consisting of 5 mM NaHCO$_3$ and 0.5 M Na$_2$SO$_4$. Due to the complementary potential windows of N-doped RGO and GMn80, both materials exhibit ideal capacitive behavior in the testing electrolyte. Accordingly, an asymmetric cell consisting of an N-doped RGO anode and a GMn80 cathode should show the typical capacitor behavior. Note that E_{OCP} of N-doped RGO and GMn80 is approximately the same (0.08 V against Ag/AgCl), meanwhile the specific capacitance of N-doped RGO and GMn80 is equal to 116.3 and 197.9 F g^{-1}, at a scan rate of 10 mV s^{-1}, respectively. Accordingly, the mass ratio between anode and cathode was adjusted to be 1.47 in order to maintain the charge balance on both electrodes. Fig. 7b shows the typical constant-current charge–discharge curves of such an asymmetric cell in the electrolyte consisting of 5 mM NaHCO$_3$ and 0.5 M Na$_2$SO$_4$ by varying the cell voltage from 1.6 to 2.0 V. Clearly, all charge–discharge curves are highly symmetric, attributable to the intrinsic reversibility of N-doped RGO and GMn80 in the testing electrolyte (see Fig. 7a). The iR drop for this asymmetric cell is also small by varying the current density of charge–discharge from 1.2 to 24 A g^{-1}, shown in Fig. 7c. All the above results demonstrate the successful assembly of an asymmetric supercapacitor consisting of an N-doped RGO anode and a GMn80 cathode with a cell voltage as large as 2 V in aqueous electrolytes.

Again, the energy and power densities of this asymmetric cell can be evaluated on the basis of Eqs. (2) and (3). Based on the total mass of all active materials, the energy and power densities of this device respectively decrease and increase from ca. 17.8 Wh kg^{-1} and 1.2 kW kg^{-1} to 11.11 Wh kg^{-1} and 23.5 kW kg^{-1}, respectively, when the current density of charge–discharge is increased from 1.2 to 24 A g^{-1}. From the Ragone plot in Fig. 7d, the five points corresponding to this asymmetric cell surmount the normal performance region of typical supercapacitors. This result reveals the great enhancements in both energy and power densities through the asymmetric design in comparison with the symmetric supercapacitor consisting of GMn80 only. Moreover, due to the excellent reversibility of both N-doped RGO and GMn80 in the testing electrolyte, no obvious loss in the current efficiency is found for this unique asymmetric design.
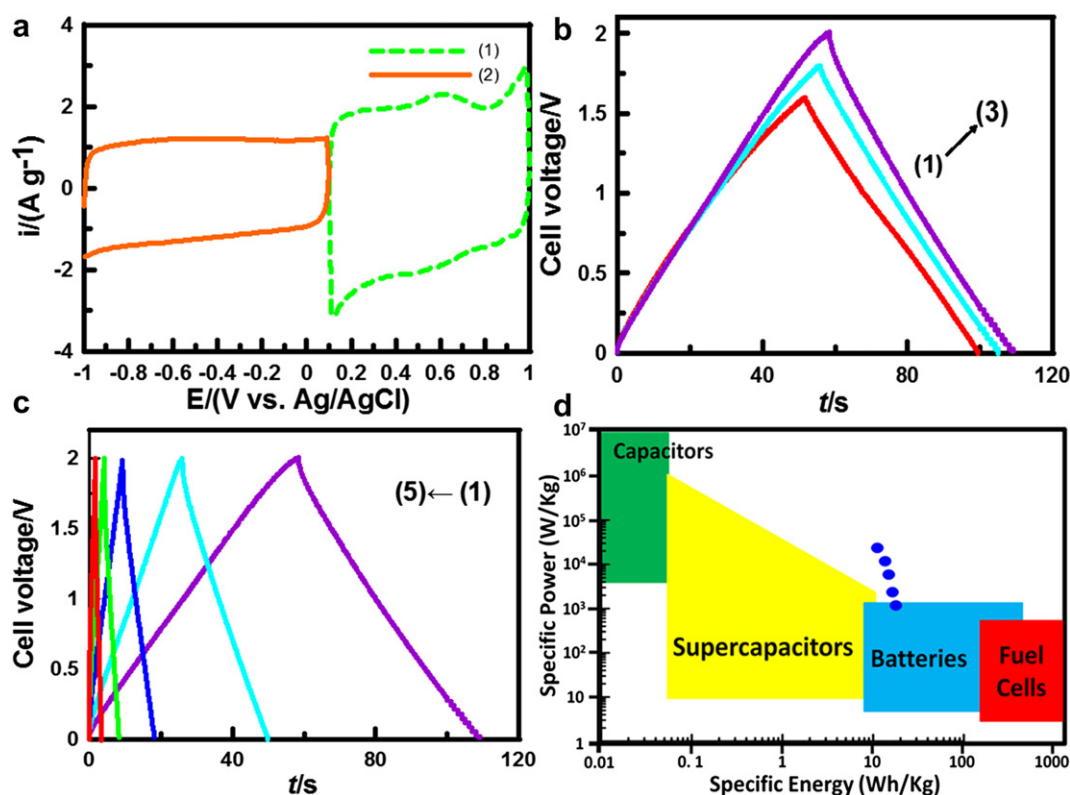
Fig. 7. (a) Cyclic voltammograms of (1) GMn80 and (2) N-doped RGO in 0.5 M Na$_2$SO$_4$ + 5 mM NaHCO$_3$ at 10 mV s^{-1}; (b,c) the constant-current charge–discharge profiles of an asymmetric supercapacitor consisting of a GMn80 cathode and an N-doped RGO anode (b) with the cell voltage of (1) 1.6, (2) 1.8, (3) 2.0 V at 1.2 A g^{-1} and (c) with a cell voltage of 2.0 V at (1) 1.2, (2) 2.4, (3) 6, (4) 12, and (5) 24 A g^{-1}. (d) The Ragone plot of an asymmetric supercapacitor consisting of a GMn80 cathode and an N-doped RGO anode (blue dots). (For interpretation of the references to color in this figure legend, the reader is referred to the web version of this article.)

4. Conclusions

From the XRD patterns, the amount of Mn$_3$O$_4$ nanocrystals in the Mn$_3$O$_4$/RGO composites can be easily controlled by the time-saving MAHS method. GMn80 with ca. 20 wt% RGO is the optimal composite with the excellent conductive networks of electrons and electrolyte. This Mn$_3$O$_4$/RGO composite shows 81% capacitance retention when the scan rate is changed from 25 to 1000 mV s^{-1} and the highest total specific capacitance ($\sim$193 F g^{-1}). In comparing with the results from a symmetric supercapacitor consisting of GMn80 only, the asymmetric supercapacitor consisting of a GMn80 cathode and an N-doped RGO anode shows the promising enhancements in both energy and power densities, e.g., ca. 11.11 Wh kg^{-1} and 23.5 kW kg^{-1}, respectively, at a charge–discharge current density of 24 A g^{-1}, demonstrating the characteristics of the next generation supercapacitors.

References

[1] T. Yamashita, A. Vannice, J. Catal. 161 (1996) 254.
[2] O. Giraldo, S.L. Brock, W.S. Willis, M. Marquez, S.L. Suib, S. Ching, J. Am. Chem. Soc. 122 (2000) 9330.
[3] Y.F. Shen, R.P. Zerger, R.N. Deguzman, S.L. Suib, L. Mccurdy, D.I. Potter, C.L. Oyoung, Science 206 (1993) 511.
[4] W.S. Seo, H.H. Jo, K. Lee, B. Kim, S.J. Oh, J.T. Park, Angew. Chem., Int. Ed. 43 (2004) 1115.
[5] C.C. Hu, T.W. Tsou, Electrochem. Commun. 4 (2002) 105.
[6] J. Junhua, K. Anthony, Electrochim. Acta 47 (2002) 2381.
[7] K.S. Park, M.H. Cho, S.H. Park, K.S. Nahm, Y.K. Sun, Y.S. Lee, M. Yoshio, Electrochim. Acta 47 (2002) 2937.
[8] M. Toupin, T. Brousse, D. Belanger, Chem. Mater. 16 (2004) 3184.
[9] H.Y. Lee, S.W. Kim, H.Y. Lee, Electrochem. Solid State Lett. 4 (2001) 19.
[10] C.C. Hu, C.C. Wang, J. Electrochem. Soc. 150 (2003) 1079.
[11] C.C. Hu, W.C. Chen, K.H. Chang, J. Electrochem. Soc. 151 (2004) 281.
[12] S.L. Kuo, N.L. Wu, J. Electrochem. Soc. 153 (2006) 1317.
[13] C.C. Hu, Y.T. Wu, K.H. Chang, Chem. Mater. 20 (2008) 2890–2894.
[14] J. Gao, M.A. Lowe, H.D. Abruna, Chem. Mater. 23 (2011) 3223–3227.
[15] M.C. Bernard, H.L. Goff, B.V. Thi, J. Electrochem. Soc. 140 (1993) 3065.
[16] A.H. De Vries, L. Hozoi, R. Broer, Phys. Rev. 66 (2002) 35108.
[17] Y. Yamashita, K. Mukai, J. Yoshinobu, M. Lippmaa, T. Kinoshita, M. Kawasaki, Surf. Sci. 514 (2002) 54.
[18] L.L. Chen, X.L. Wu, Y.G. Guo, Q.S. Kong, Y.Z. Xia, J. Nanosci. Nanotechnol. 10 (2010) 8158–8163.
[19] F. Zhang, X.G. Zhang, L. Hao, Mater. Chem. Phys. 126 (2011) 853–858.
[20] S. Xing, Z. Zhou, Z. Ma, Y. Wu, Mater. Lett. 65 (2011) 517–519.
[21] A.K. Geim, K.S. Novoselov, Nat. Mater. 6 (2007) 183.
[22] C. Si, E.T. Samulski, Nano Lett. 8 (2008) 1679.
[23] W. Hong, Y. Xu, G. Lu, C. Li, G. Shi, Electrochem. Commun. 10 (1555).
[24] T.Y. Kim, H.W. Lee, M. Stoller, D.R. Dreyer, C.W. Bielawski, R.S. Ruoff, K.S. Suh, ACS Nano. 5 (2011) 436.
[25] Z.S. Wu, D.W. Wang, W. Ren, J. Zhao, G. Zhou, F. Li, et al., Adv. Funct. Mater. 20 (2010) 3595–3602.
[26] B. Wang, J. Park, C. Wang, H. Ahn, G. Wang, Electrochim. Acta 55 (2010) 6812–6817.
[27] J. Yan, Z. Fan, T. Wei, W. Qian, M. Zhang, F. Wei, Carbon 48 (2010) 3825–3833.
[28] A. Izadi-Najafabadi, S. Yasuda, K. Kobashi, T. Yamada, D.N. Futaba, H. Hatori, M. Yumura, S. Iijima, K. Hata, Adv. Mater. 22 (2010) 235.
[29] T. Brousse, P.L. Taberna, O. Crosnier, R. Dugas, P. Guillemet, Y. Scudeller, Y. Zhou, F. Favier, D. Bélanger, P. Simon, J. Power Sources 173 (2007) 633–641.
[30] Y.G. Wang, Y.Y. Xia, Electrochem. Commun. 7 (2005) 1138.
[31] P.C. Chen, G.Z. Shen, Y. Shi, H.T. Chen, C.W. Zhou, ACS Nano. 4 (2010) 4403.
[32] Z.S. Wu, W. Ren, D.W. Wang, F. Li, B. Liu, H.M. Cheng, ACS Nano. 4 (2010) 5835.
[33] Q. Qu, Y. Shi, L. Li, W. Guo, Y. Wu, H. Zhang, S. Guan, R. Holze, Electrochem. Commun. 11 (2009) 1325–1328.

[34] T. Cottineau, M. Toupin, T. Delahaye, T. Brousse, D. Bélanger, Appl. Phys. 82 (2006) 599–606.
[35] H. Wendt, Electrochim. Acta 29 (1991) 1513–1525.
[36] C.C. Hu, C.H. Chu, J. Electroanal. Chem. 503 (2001) 105.
[37] C.C. Hu, W.Y. Li, J.Y. Lin, J. Power Sources 137 (2004) 152.
[38] E.A. Muller, L.F. Rull, L.F. Vega, K.E. Gubbins, J. Phys. Chem. 100 (1996) 1189–1196.
[39] T. Ohba, H. Kanoh, K. Kaneko, J. Am. Chem. Soc. 126 (2004) 1560–1562.
[40] M. Ocaña, Colloid Polym. Sci. 278 (2000) 443.
[41] K.H. Chang, C.C. Hu, Chem. Mater. 19 (2007) 2112.
[42] S. Komaba, A. Ogata, T. Tsuchikawa, Electrochem. Commun. 10 (2008) 1435.
[43] S. Yoon, C. Lee, S.M. Oh, Y.K. Park, W.C. Choi, J. Non Cryst. Solids 355 (2009) 252–256.
[44] J.N. Broughton, M.J. Brett, Electrochim. Acta 50 (2005) 4814.
[45] N. Nagarajan, M. Cheong, I. Zhitomirsky, Mater. Chem. Phys. 103 (2007) 47.
[46] Y.K. Zhou, M. Toupin, D. Bélanger, T. Brousse, F. Favier, J. Phys. Chem. Solids 67 (2006) 1351.
[47] D.P. Dubal, D.S. Dhawale, R.R. Salunkhe, S.M. Pawar, C.D. Lokhande, Appl. Surf. Sci. 256 (2010) 4411–4416.
[48] T.P. Gujar, V.R. Shinde, C.D. Lokhande, W.Y. Kim, K.D. Jung, O.S. Joo, Electrochem. Commun. 9 (2007) 504.
[49] T. Brousse, M. Toupin, R. Dugas, L. Athouel, O. Crosnier, D. Bélanger, J. Electrochem. Soc. 153 (2006) 2171–2180.
[50] E. Beaudrouet, A. Le Gal La Salle, D. Guyomard, Electrochim. Acta 54 (2009) 1240–1248.
[51] S. Ardizzone, G. Fregonara, S. Trasatti, Electrochim. Acta 35 (1990) 263.
[52] T. Liu, W.G. Pell, B.E. Conway, Electrochim. Acta 42 (1997) 3541.
[53] K.H. Chang, Y.T. Wu, C.C. Hu, in: V. Gupta (Ed.), Recent Advances in Supercapacitors, Transworld Research Network, Kerala, India, 2006, pp. 29–56 (Chapter 3).
[54] K. Naoi, P. Simon, Interface 17 (2008) 34.
[55] J.R. Miller, A.F. Burke, Interface 17 (2008) 53.
[56] A.V. Murugan, T. Muraliganth, A. Manthiram, Chem. Mater. 21 (2009) 5004.
[57] Y.H. Chu, K.H. Chang, C.C. Hu, Electrochim. Acta 61 (2012) 124–131.